Progress on Flutter Analysis of the X-56A for the Third Aeroelastic Prediction Workshop

Steven J. Massey,* Bret K. Stanford,† and Kevin E. Jacobson‡
NASA Langley Research Center, Hampton, VA, 23681

An aeroelastic analysis is presented for the X-56A test case of the upcoming third aeroelastic prediction workshop. Results using the FUN3D linearized frequency-domain solver are shown for four different structural models corresponding to increasing fuel loads. The present study is blind since only redacted and normalized flight test data have been published. However, trends in body-freedom flutter mode frequencies and damping with respect to fuel load are seen to agree well with previously published redacted flight test data.

Fig. 1 X-56A Multi-Utility Technology Testbed (MUTT), NASA Photo / Jim Ross.

I. Introduction

In support of the third Aeroelastic Prediction Workshop (AePW-3)§, a progress report of the ongoing aeroelastic computations of the X-56A (Fig. 1) test case is presented. A joint publication and special sessions for AePW-3 are scheduled for AIAA SciTech 2023. Within the AePW-3 there are four focus areas of interest: transonic flutter including shock buffet, hypersonic aeroelasticity, geometrically nonlinear wing deflections at low speed, and prediction and control of body-freedom flutter (BFF). The subject of this study is the prediction of BFF, as well as, all other flutter modes for the X-56A aircraft using the FUN3D [1] Navier-Stokes solver. The X-56A, also known as the Multi-Utility Technology Testbed (MUTT) [2] is a 15% scale remotely piloted aircraft that was built to study the physics of BFF and develop active control solutions for it. Body-freedom flutter arises from an interaction of a vehicle's flexible structural modes and its rigid flight dynamic modes. For high aspect ratio flying wings in general [3] and the X-56A in particular [4], it is the coupling of the short period flight dynamic mode with the symmetric first bending structural mode that results in BFF. With the recent addition [5] of a linearized frequency-domain (LFD) solver to augment FUN3D's existing [6] aeroelastic capabilities, rigid body modes can now be included in flutter analysis, thus making BFF prediction possible with FUN3D.

---

*Research Aerospace Engineer, Aeroelasticity Branch, MS 340, steven.j.massey@nasa.gov, Senior Member AIAA.

†Research Aerospace Engineer, Aeroelasticity Branch, MS 340, Associate Fellow AIAA.

‡Research Aerospace Engineer, Aeroelasticity Branch, MS 340, Member AIAA.

§https://nescacademy.nasa.gov/workshops/AePW3/public [accessed 3 May 2021]

II. Methodology

A. Finite Element Model and CFD Mesh

The solution process starts with a finite element structural model (FEM) [*] tuned using data from ground vibration tests [7]. A normal modes analysis is then performed in Nastran [8]. These natural vibration modes are then interpolated to the CFD surface mesh using radial basis functions [†]. The CFD surface was created from CAD distributed by AePW-3. The provided OML CAD does not contain engines, landing gear and other details included in the FEM and that are present on the as-flown configuration. Where possible, mode shapes of components not represented in the CFD mesh were not included in the analysis. A family of three CFD meshes were created with Pointwise [9] with nominal maximum surface cell edge lengths of 1.0, 0.5, and 0.25 inches, all with wall spacing of $y^+ \approx 1$. The resultant meshes contain 3.4M, 7.2M, 29.7M nodes, respectively, as shown in Fig. 2.

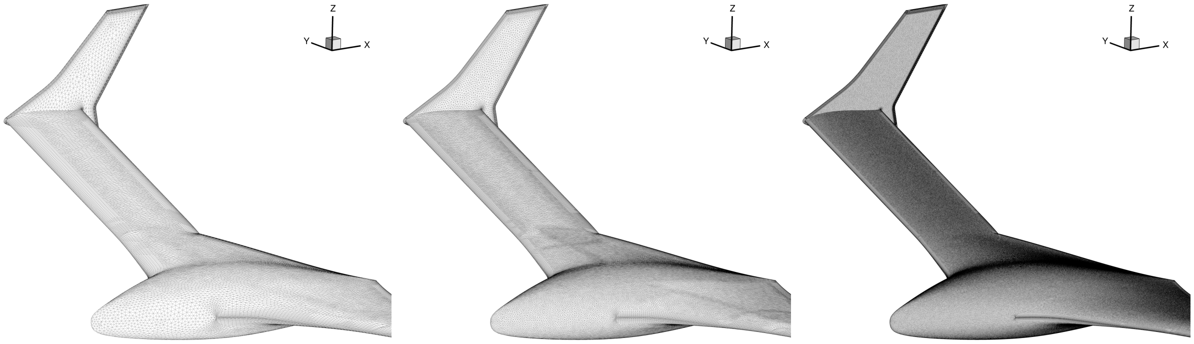

(a) 3.4M nodes, nominal 1 inch spacing. (b) 7.2M nodes, nominal 0.5 inch spacing. (c) 29.7M nodes, nominal 0.25 inch spacing.

Fig. 2 Coarse, medium and fine surface meshes.

B. FUN3D Solver Details

Solutions to the Reynolds-averaged Navier-Stokes equations are computed using the FUN3D flow solver. All solid surfaces are modeled with no-slip boundary conditions and far-field boundaries are of the Riemann invariant type. Turbulence closure is obtained using the Spalart-Allmaras [10] one-equation model with the quadratic constitutive relation Reynolds stress model of Spalart [11] and the Spalart-Shur rotation/curvature correction [12]. Inviscid fluxes are computed using the Roe scheme [13]. For second-order spatial accuracy, interface values required for Roe's scheme are reconstructed using gradients at grid nodes obtained by a least-squares technique. For the mixed prismatic/tetrahedral grids used in this study, the viscous fluxes are evaluated to second-order accuracy using a combination of edge-based and Green-Gauss gradients. In high gradient regions of the flow, limiters on these reconstructed values may be needed for stability. However, in the present computations, no limiters were required. Time integration is accomplished by an Euler implicit backward difference scheme with dual time stepping to achieve second-order accuracy [14, 15].

Grid motion due to aeroelastic deformations is carried out by treating the CFD grid as a linear elastic medium with material properties based on the grid characteristics with appropriate application of the geometric conservation law [16]. In the present computations, the modulus of elasticity is boosted near the wing by setting it to vary with the inverse of the square of the distance away from the wing surface, thereby increasing the robustness of the grid motion.

The structural deformations are computed internally using a linear modal method, which was implemented in FUN3D by Biedron and Thomas [6] following the approach used in CAP-TSD [17]. The LFD solver is implemented [5] in the stabilized finite element solver (SFE) path of FUN3D [18]. The LFD solver linearizes the flow about a base static aeroelastic state via rigid body and flexible mode shapes over a range of reduced frequencies between 0.0 and 2.0. The static aeroelastic state is computed using only flexible modes and either the finite volume (FV) or SFE solvers. For the present results, the FV solver was used to maintain compatibility with the existing time-domain workflow, however, it is expected that starting the LFD solver from an SFE solution would result in better convergence properties and will be

---

[*] The FEM and OML CAD were cleared by AFRL for public release under case number 88ABW-2013-4832.

[†] Open source software available from https://software.nasa.gov/software/LAR-19607-1.

used for the final workshop results. The final product of the LFD solver is a matrix of generalized aerodynamic forces (GAFs). A noniterative [19], *p–k* [20] flutter eigensolver is then used to compute the flutter envelope.

Though it is known [3] that BFF of flying wing configurations is captured well with fully linear aerodynamics and structures, the power of LFD is its ability to compute time linearized unsteady aerodynamics about any nonlinear aeroelastic state. Thus, the value of this study is to verify LFD for BFF against lower fidelity tools where they should agree, as well as, validate against unredacted flight data when it becomes available. The present LFD implementation has already been shown to accurately predict flutter [5, 21–23] in the transonic flow regime where linear aerodynamics are insufficient.

III. Results

The present results are based on a freestream velocity of 100 knots at standard sea-level conditions, which corresponds to a Mach number of 0.15 and dynamic pressure of 0.235 psi. Initial computations found an angle of attack of 0.27° sufficient to trim the vehicle at the static aeroelastic condition for the 10 lb fuel load. At this trim angle, no significant effect on flutter speed was observed, thus all results presented are at zero angle of attack. Also, additional freestream dynamic pressures were used to compute the static aeroelastic state for LFD and were found not to significantly affect predicted flutter speeds. The effect of mesh refinement on the static aeroelastic state is fairly minimal in terms of integrated loads (Table 1) and surface pressures and deformation (Fig. 3).

As designed [2], three flutter modes are present in the results: body-freedom flutter (BFF), symmetric wing bending/torsion (SWBT), and antisymmetric wing bending/torsion (AWBT). These flutter modes are shown in Fig. 4, with the jig shape in gray and the flutter mode shape colors corresponding to those in Fig. 5. In Fig. 5, LFD results showing the effect of mesh refinement are plotted along with Nastran results for damping vs velocity (V–g) and frequency vs velocity(V–f) for the 10 lb fuel case. Corresponding flutter speeds are listed in Table 2. The results for the coarse and medium meshes are seen to agree with each other exceptionally well, while the fine mesh solution departs from the other meshes primarily in the BFF mode. Nastran results are seen to match coarse and medium LFD results for BFF and begin to depart from LFD results for all meshes for speeds higher than 150 KEAS (equivalent airspeed in knots). Given the similarity of the base static aeroelastic deflection state across meshes, it is suspected that the grid sensitivity observed in the LFD results is due to differing levels of convergence caused by restarting from a solution generated with the FV solver instead of the SFE solver.

Table 1 Effect of mesh refinement on lift, drag, and pitching moment coefficients for the static aeroelastic condition.

Mesh	C_L	C_D	C_m
Coarse	0.1574	0.0199	0.0231
Medium	0.1595	0.0182	0.0229
Fine	0.1635	0.0160	0.0216

Table 2 Effect of mesh refinement on flutter equivalent airspeed in knots (KEAS)

Case	BFF	SWBT	AWBT
LFD Coarse	123.6	156.6	187.6
LFD Medium	123.9	156.5	187.3
LFD Fine	118.4	156.3	186.6
Nastran	122.8	152.5	182.8

The effect of fuel load on the damping of the primary modes involved in flutter are shown for the medium mesh and Nastran in Figure 6. For both LFD and Nastran results, as fuel load increases, damping increases for the short period mode resulting in higher BFF flutter speeds, while SWBT and AWBT flutter speeds are virtually unchanged, see also Table 3. Damping in symmetric wing first bending (SW1B) shows slight mixed changes, while antisymmetric wing first bending (AW1B), symmetric wing first torsion (SW1T), and antisymmetric wing first torsion (AW1T) modes are largely unaffected. The same sensitivity to fuel load is reflected in frequency in Fig. 7, where the frequency of the short period mode is seen to decrease with increasing fuel load. A summary of the effects of fuel load on stability and frequency can be seen in the root locus plots for LFD and Nastran results, Fig. 8, where the BFF occurs at a higher frequency and becomes less unstable with increased fuel load and the symmetric and antisymmetric wing bending/torsion flutter mechanism are insensitive to fuel load.

Finally, it was assumed that only the BFF mode wouldn't be found in the time domain analysis because of its rigid body mode dependence. However, in exploratory time domain computations, the SWBT and AWBT flutter modes were also absent. Because all rigid modes are neglected in the time domain, Nastran and LFD computations were repeated without rigid body modes and were in good agreement with each other and also did not exhibit any flutter modes, with the possible exception of LFD SWBT which just barely becomes unstable at 230 KEAS, see Fig. 9. Close examination of the fuselage region the flutter mode shapes in Fig. 4, indicate that SWBT mode likely contains a vertical translation rigid mode component while the AWBT mode contains a rolling mode contribution. The rigid modes in the current modal decomposition are linear combinations of translations and rotations about the principal axes, which prevents isolating these modes to verify their contributions. In follow-on computations, an alternative normal mode decomposition will be used to recover rigid modes about the principal axes for further analysis.

Table 3 Effect of fuel load on flutter speed in KEAS

	LFD Medium Mesh			Nastran		
Case	BFF	SWBT	AWBT	BFF	SWBT	AWBT
10 lb	123.9	156.5	187.3	122.8	152.5	182.8
30 lb	129.1	156.4	186.8	126.1	152.4	182.2
60 lb	142.6	156.3	186.2	133.1	152.3	181.4
80 lb	159.7	156.3	185.7	136.5	152.3	180.9

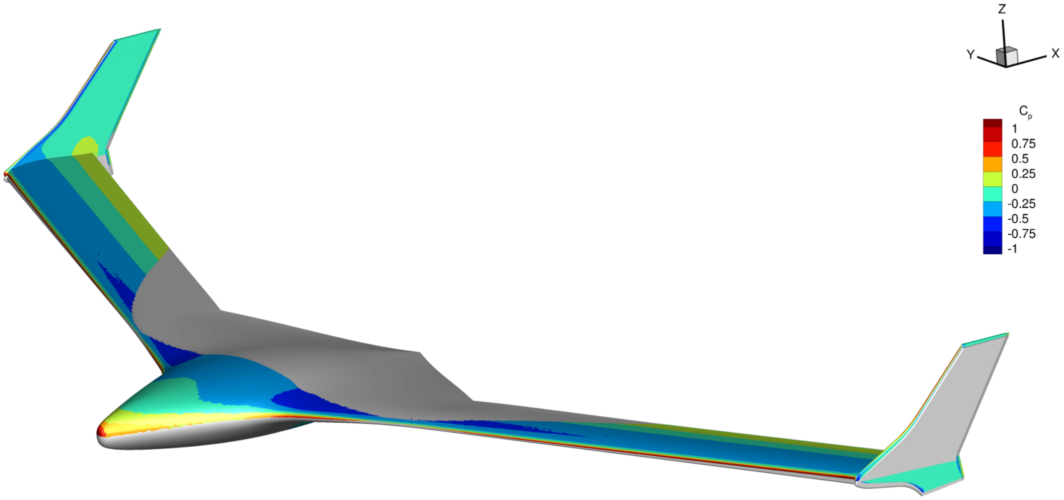

(a) Coarse

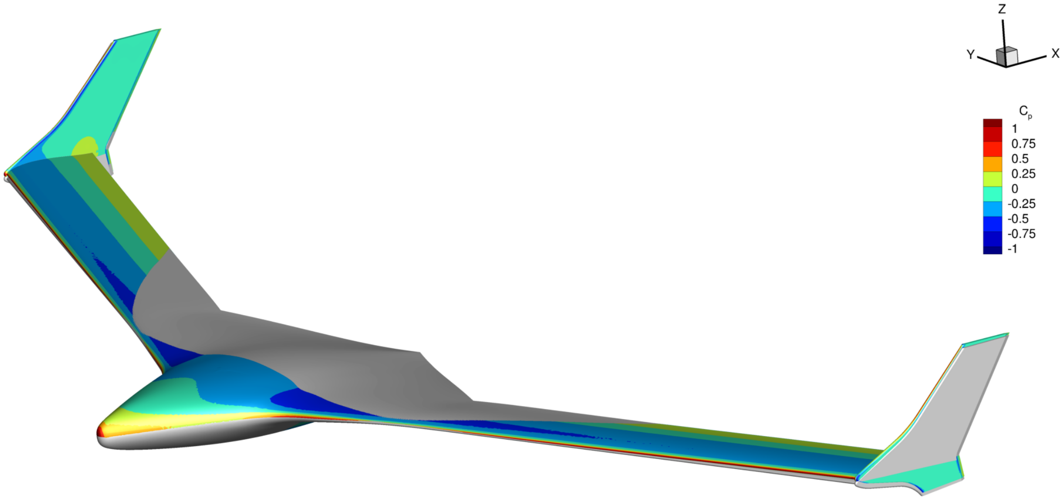

(b) Medium

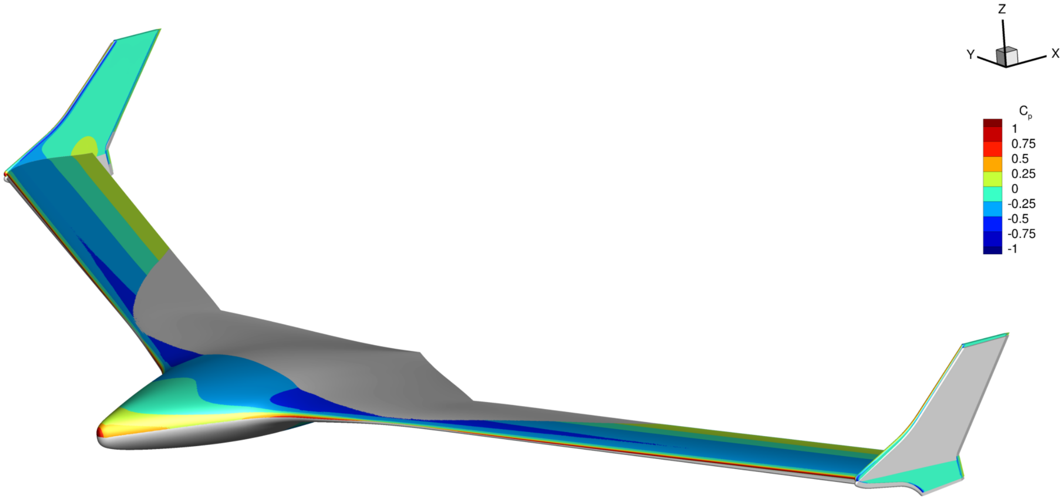

(c) Fine

Fig. 3 Effect of mesh refinement on static deformation and surface pressure, jig shape shown in gray.

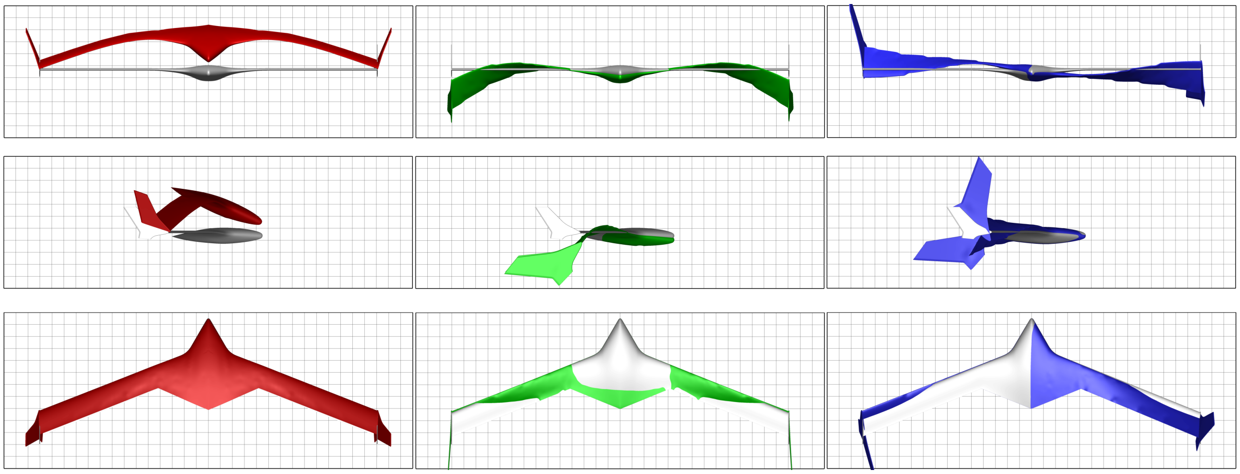

(a) BFF (b) SWBT (c) AWBT

Fig. 4 Flutter mode shapes with jig shape in gray.

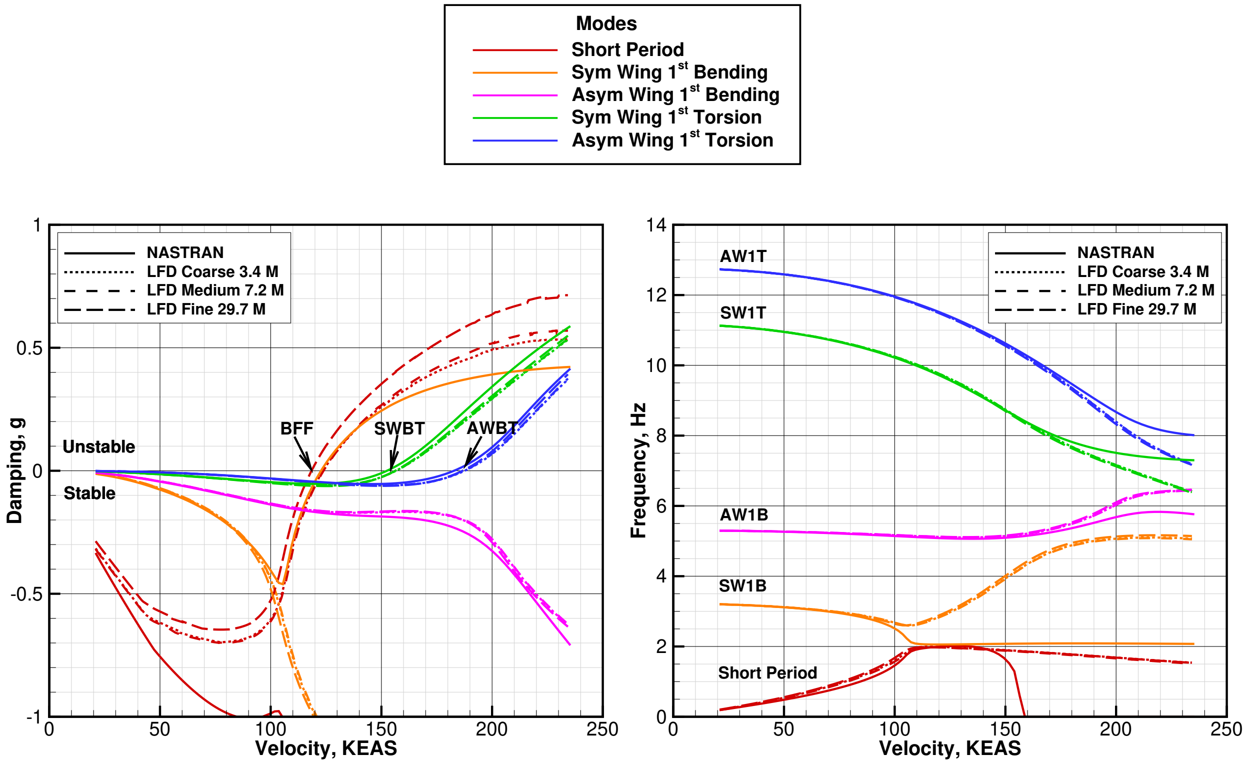

(a) V-g. (b) V-f.

Fig. 5 Effect of mesh refinement on primary modes involved in flutter for 10 lb fuel case for LFD compared with Nastran results.

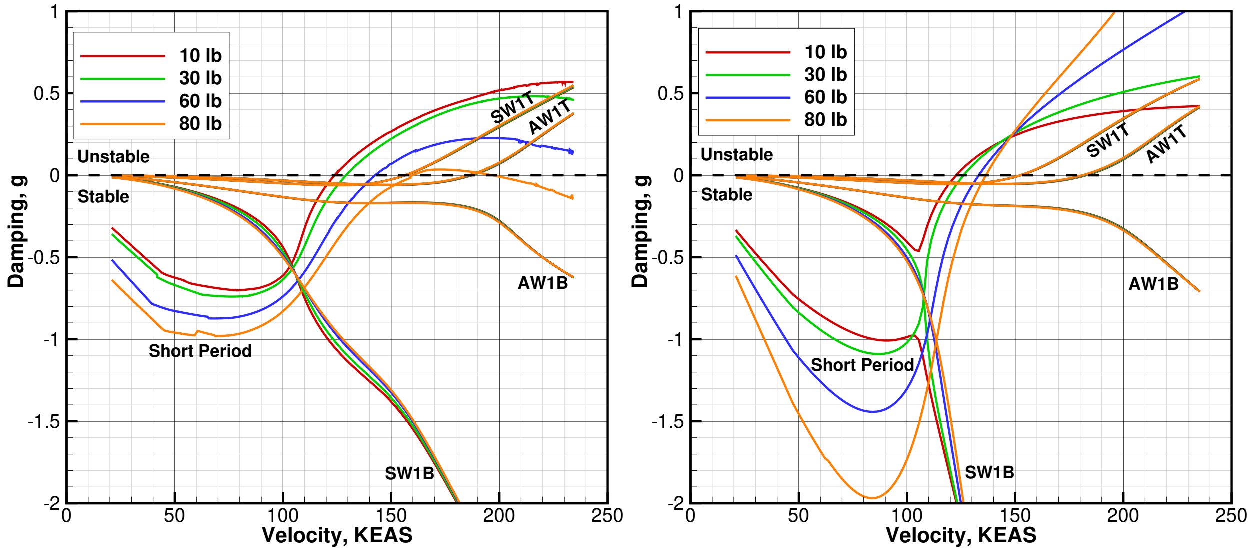

(a) LFD medium mesh.

(b) Nastran.

Fig. 6 Effect of fuel load on damping of primary modes.

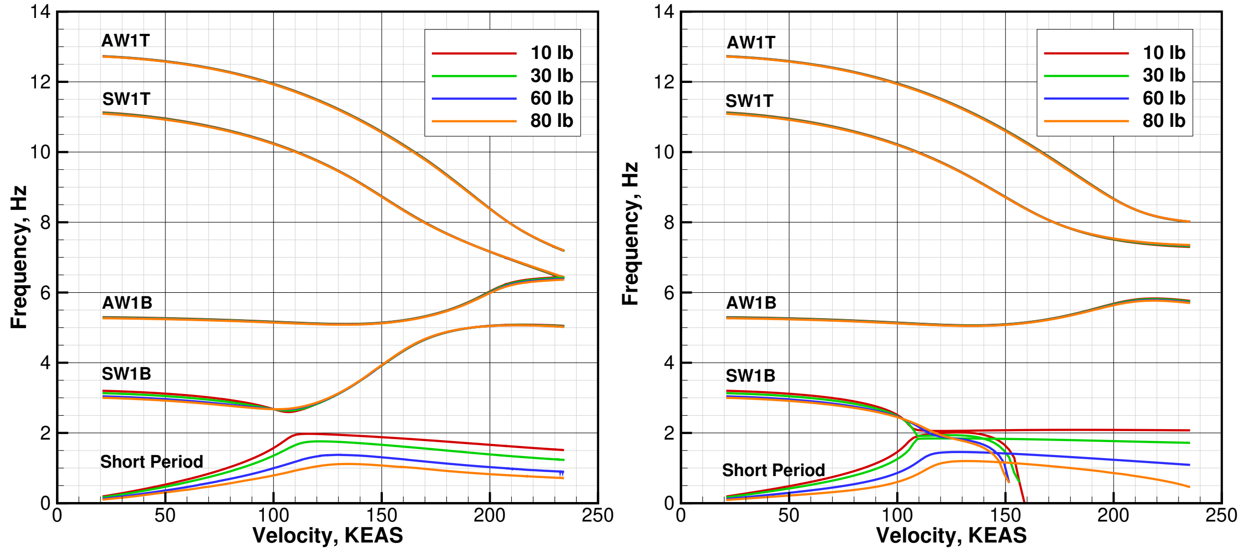

(a) LFD medium mesh.

(b) Nastran.

Fig. 7 Effect of fuel load on frequency of primary modes.

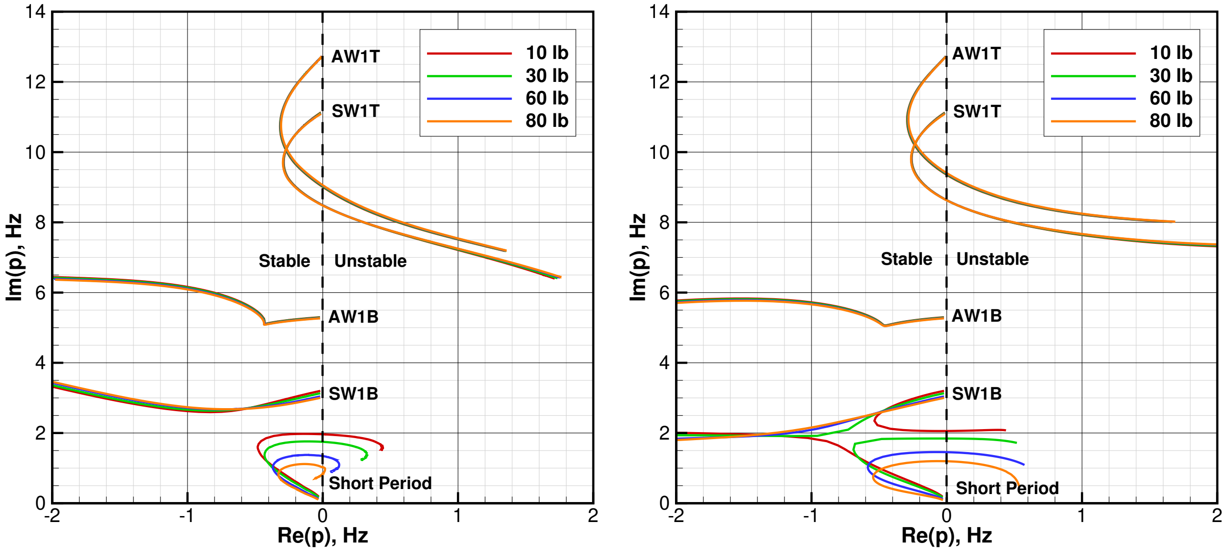

(a) LFD medium mesh.

(b) Nastran.

Fig. 8 Effect of fuel load on root locus of primary modes.

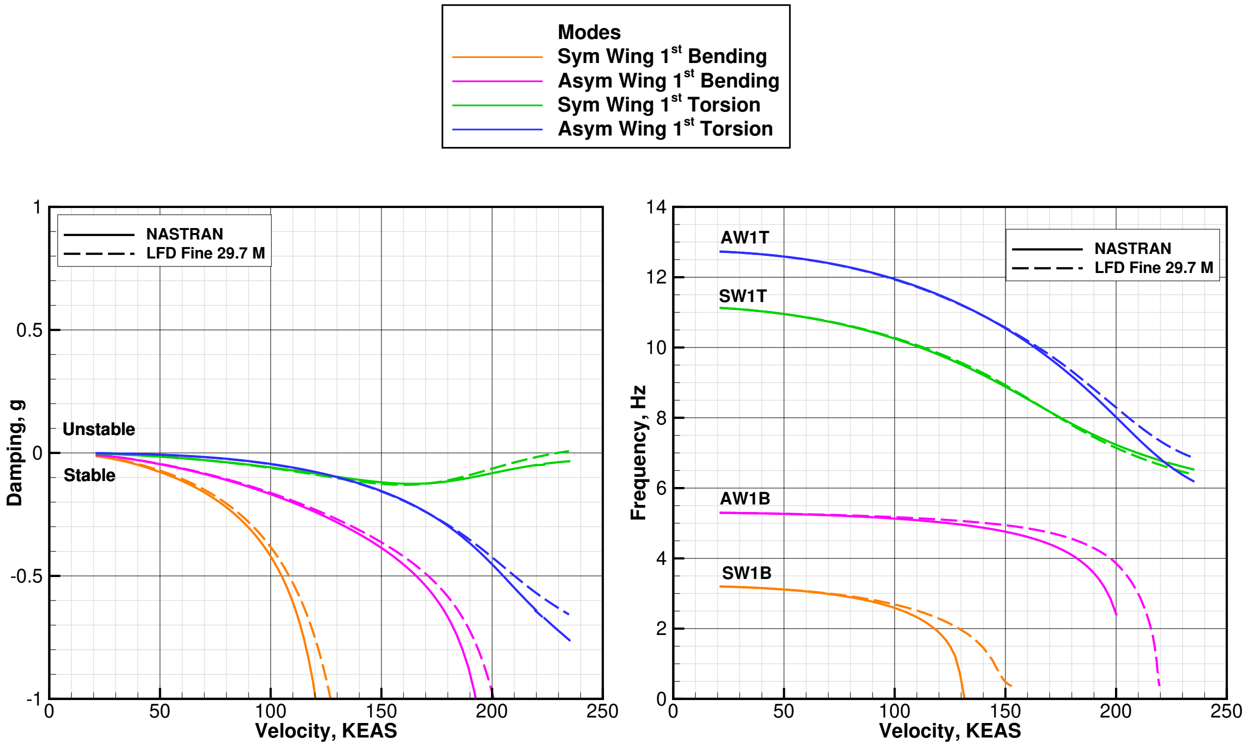

(a) V-g.

(b) V-f.

Fig. 9 Effect of neglecting all rigid body modes on flutter.

IV. Concluding Remarks

A progress report on the ongoing X-56A aeroelastic analysis for the 2023 Aeroelastic Prediction Workshop was presented. Results using the FUN3D linearized frequency-domain solver and Nastran were presented for four different structural models corresponding to increasing fuel loads. Nastran and LFD results were generally in good agreement with each other. The results for the coarse and medium meshes agreed with each other exceptionally well, while the fine mesh solution departed from the other meshes primarily in the BFF mode. Nastran results were seen to match coarse and medium LFD results for BFF and began to depart from LFD results for all meshes for speeds higher than 150 KEAS. For the final workshop paper, a further analysis of mesh convergence will be conducted using only the SFE solver. Trends in body-freedom flutter mode frequencies and damping with respect to fuel load agree with published flight-test data [4] and computations [7], though quantitative comparisons are difficult at this point because previously published data were redacted or normalized and the current FEM has been further updated. The AePW-3 workshop will eventually release flight data, but for these initial computations, blind comparisons are sought. The FUN3D LFD solver has proven to be very capable of predicting body-freedom flutter, which is a new capability for FUN3D-based aeroelasticity.

Acknowledgments

This work is supported by the Transformational Tools and Technologies (TTT) project of the NASA Transformative Aeronautics Concepts Program (TACP).

References

[1] Biedron, R. T., Carlson, J., Derlaga, J. M., Gnoffo, P. A., Hammond, D. P., Jacobson, K. E., Jones, W. T., Kleb, B., Lee-Rausch, E. M., Nielsen, E. J., Park, M. A., Rumsey, C. L., Thomas, J. L., Thompson, K. B., Walden, A. C., Wang, L., and Wood, W. A., "FUN3D Manual: 13.7," NASA TM 2020–5010139, Nov. 2020.

[2] Beranek, J., Nicolai, L., Buonanno, M., Burnett, E., Atkinson, C., and Holm-Hansen, B., "Conceptual Design of a Multi-utility Aeroelastic Demonstrator," AIAA Paper 2010–9350, Sep. 2010. https://doi.org/10.2514/6.2010-9350.

[3] Love, M. H., Zink, P. S., Wieselmann, P. A., and Youngren, H., "Body Freedom Flutter of High Aspect Ratio Flying Wings," AIAA Paper 2005–1947, Apr. 2005. https://doi.org/10.2514/6.2005-1947.

[4] Ouellette, J., and Valdez, F. D., "Generation and Calibration of Linear Models of Aircraft with Highly Coupled Aeroelastic and Flight Dynamics," AIAA Paper 2020–1016, Jan. 2020. https://doi.org/10.2514/6.2020-1016.

[5] Jacobson, K. E., Stanford, B. K., Wood, S. L., and Anderson, W. K., "Flutter Analysis with Stabilized Finite Elements based on the Linearized Frequency-domain Approach," AIAA Paper 2020–0403, Jan. 2020. https://doi.org/10.2514/6.2020-0403.

[6] Biedron, R. T., and Thomas, J. L., "Recent Enhancements To The FUN3D Flow Solver For Moving-Mesh Applications," AIAA Paper 2009–1360, Jan. 2009. https://doi.org/10.2514/2009-1360.

[7] Pak, C., and Truong, S., "Creating a Test-Validated Finite-Element Model of the X-56A Aircraft Structure," *Journal of Aircraft*, Vol. 52, No. 5, 2015, pp. 1644–1667. https://doi.org/10.2514/1.C033043.

[8] Rodden, W., and Johnson, E., *MSC/NASTRAN Aeroelastic Analysis User's Guide*, MacNeal-Schwendler, Los Angeles, 1994.

[9] *Pointwise V18.4R3 User Manual*, Pointwise, Inc., Fort Worth, Texas, 2021.

[10] Spalart, P. R., and Allmaras, S. R., "A One-Equation Turbulence Model for Aerodynamic Flows," *La Recherche Aerospatiale*, , No. 1, 1994, pp. 5–21.

[11] Spalart, P. R., "Strategies for Turbulence Modelling and Simulations," *International Journal of Heat and Fluid Flow*, Vol. 21, No. 3, 2000, pp. 252–263.

[12] Shur, M. L., Strelets, M. K., Travin, A. K., and Spalart, P. R., "Turbulence Modeling in Rotating and Curved Channels: Assessing the Spalart-Shur Correction," *AIAA Journal*, Vol. 38, No. 5, 2000, pp. 784–792.

[13] Roe, P. L., "Approximate Riemann Solvers, Parameter Vectors, and Difference Schemes," *Journal of Computational Physics*, Vol. 43, 1981, pp. 357–372.

[14] Nyukhtikov, M., Smelova, N., Mitchell, B. E., and Holmes, D. G., "Optimized Dual-Time Stepping Technique For Time-Accurate Navier-Stokes Calculations," *Proceedings of the 10th International Symposium on Unsteady Aerodynamics, Aeroacoustics and Aeroelasticity of Turbomachines*, 2003.

[15] Vatsa, V. N., Carpenter, M. H., and Lockard, D. P., "Re-evaluation of an Optimized Second Order Backward Difference (BDF2OPT) Scheme for Unsteady Flow Applications," AIAA Paper 2010–0122, Jan. 2010. https://doi.org/10.2514/6.2010-0122.

[16] Thomas, P. D., and Lombard, C. K., "Geometrical Conservation Law and Its Application," *AIAA Journal*, Vol. 17, No. 10, 1978, pp. 1030–1037.

[17] Cunningham, H. J., Batina, J. T., and Bennett, R. M., "Modern wing flutter analysis by computational fluid dynamics methods," *Journal of Aircraft*, Vol. 25, No. 10, 1988, pp. 962–968. https://doi.org/10.2514/3.45686.

[18] Anderson, W. K., Newman, J. C., and Karman, S. L., "Stabilized Finite Elements in FUN3D," *Journal of Aircraft*, Vol. 55, No. 2, 2018, pp. 696–714. https://doi.org/10.2514/1.C034482.

[19] van Zyl, L. H., and Maserumule, M. S., "Divergence and the p-k Flutter Equation," *Journal of Aircraft*, Vol. 38, No. 3, 2001, pp. 584–586. https://doi.org/10.2514/2.2805.

[20] Hassig, H. J., "An Approximate True Damping Solution of the Flutter Equation by Determinant Iteration." *Journal of Aircraft*, Vol. 8, No. 11, 1971, pp. 885–889. https://doi.org/10.2514/3.44311.

[21] Stanford, B. K., Jacobson, K. E., and Massey, S. J., "Transonic Aeroelastic Modeling of the NACA 0012 Benchmark Wing," AIAA Paper 2020–2716, Jun. 2020. https://doi.org/10.2514/6.2020-2716.

[22] Waite, J. M., Bartels, R. E., and Stanford, B. K., "Aeroelastic Model Development for the Integrated Adaptive Wing Technology Maturation ProjectWind-Tunnel Test," AIAA Paper 2020–2717, Jun. 2020. https://doi.org/10.2514/6.2020-2717.

[23] Jacobson, K. E., Stanford, B. K., Wood, S. L., and Anderson, W. K., "Adjoint-based Sensitivities of Flutter Predictions based on the Linearized Frequency-domain Approach," AIAA Paper 2021–0282, Jan. 2021. https://doi.org/10.2514/6.2021-0282.